Efficiency Improvement Strategy Based on Frequency Reduction With Constant Current Characteristic for Underwater Wireless Power Transfer Systems

Han Hu, Hongsheng Hu, *Member, IEEE*, Fengwei Chen, Xin Dai, *Member, IEEE*, and Yue Sun

***Abstract*—In this article, the problem of efficiency optimization for underwater wireless power transfer (UWPT) systems is considered. The main reason for efficiency degradation in UWPT systems is the eddy current loss (ECL) caused by seawater, which is proportional to the square of the system operating frequency. To alleviate ECL, an efficiency improvement strategy based on frequency reduction with constant current characteristics is developed. By introducing a constant gain frequency reduction (CGFR) module designed conformally with the magnetic coupler of the original system, the receiving coil ECL reduces. In contrast, the transmitting coil ECL remains unchanged, indicating an increase in power efficiency. The CGFR module does not need to add any additional converters or controls, nor does it rely on communication, resulting in strong universality. By circuit analysis, a simplified equivalent circuit of the proposed system is established, and the losses of the proposed system are analyzed, on this basis, the parameter configuration of the CGFR module is given. A 1.5-kW prototype with a coupling coefficient of 0.07 is built, and experimental results show that the proposed CGFR module indeed improves the efficiency when the load varies in the range of [5, 12] ohms, with a maximum increase of 7.8%. The proposed strategy can significantly improve the efficiency of the UWPT system, and it is particularly applicable in scenarios of long-distance transmission.**

***Index Terms*—Constant gain, eddy current loss (ECL), efficiency improvement, frequency reduction, underwater wireless power transfer (UWPT).**

I. Introduction

AUTONOMOUS underwater vehicles (AUVs) are widely used in marine resource exploration and underwater cable inspection. However, the battery capacity limits the endurance of AUVs and battery charging becomes an important problem. Compared with the traditional plug-in power supply methods, the wireless power transfer (WPT) technology has the advantages of safety, noncontact operation, and long service life and, thus, is more suitable for underwater charging of AUVs. Among various WPT technologies, the inductive power transfer (IPT) technology has been widely applied in many fields such as electric vehicles, biomedical treatment, and household appliances due to its higher transmission efficiency [1].

However, the IPT system faces numerous challenges in the seawater environment. Scholars have carried out a series of studies on these challenges, which can be roughly divided into the following three categories.

1) Misalignment of magnetic coupler caused by ocean currents can be solved by designing an antimisalignment magnetic coupler [2], [3], [4], [5], [6], designing the circuit topology [7], or adding a variable inductor [8].
2) System parameter drift caused by seawater medium can be solved by parameter identification and frequency regulation [9], [10], [11].
3) Lower efficiency caused by the eddy current losses (ECL) can be solved by changing the structure of magnetic coupler [12], [13], or optimizing circuit parameters [14], [15].

Among the abovementioned three types of studies, lower efficiency is the key problem affecting the underwater application of the IPT system [16]. Therefore, this article will conduct further research on improving the transmission efficiency of the underwater WPT (UWPT) system. A $1 \times 1 \times 1$ magnetic coupler is proposed in [12], which is able to reduce by half the transmitting (Tx) coil ECL. However, this method cannot be applied to situations where the receiving (Rx) coil uses ferrite. To circumvent the above drawback, an integrated magnetic-electric coupler is proposed in [13], which can transmit power through both magnetic and electric fields simultaneously. This design improves the efficiency since the capacitance-coupled route does not generate ECL, but at the price of a more complicated parameter design procedure. In [14], the ECL can be reduced by suitably adjusting the phase difference between the currents flowing through Tx and Rx coils. Nevertheless, an active rectifier is required on the Rx side and the control of the system is complicated. In [15], expressions characterizing the relationship between the electric field intensity and the ECL are derived, showing that the efficiency can be improved by optimizing the operating frequency of the system. Nevertheless, the method does not guarantee a constant current (CC) gain for UWPT systems with series–series (SS) topology, resulting in weak compatibility.

Received 4 March 2025; revised 14 April 2025; accepted 24 April 2025. Date of publication 28 April 2025; date of current version 30 June 2025. This work was supported by the National Natural Science Foundation of China under Grant 52207003, Grant 62073246, and Grant 52277003. Recommended for publication by Associate Editor M. Ponce-Silva. *(Corresponding author: Hongsheng Hu.)*

The authors are with the School of Automation, Chongqing University, Chongqing 400044, China (e-mail: 20211301007@stu.cqu.edu.cn; huhongsheng@cqu.edu.cn; fengwei.chen@cqu.edu.cn; daixin@cqu.edu.cn; syue06@cqu.edu.cn).

Color versions of one or more figures in this article are available at https://doi.org/10.1109/TPEL.2025.3564961.

Digital Object Identifier 10.1109/TPEL.2025.3564961

To ensure a CC gain of the system, dc–dc converters can be cascaded at the Tx side [17], the Rx side [18], or both sides [19]. However, an additional conversion circuit will increase the system's complexity and reduce transmission efficiency. To avoid adding extra conversion circuits, an active rectifier circuit can be adopted on the Rx side [20], and the constant gain of the system can be ensured through dual side phase-shift control [21]. However, this method causes the system to operate in a nonzero-voltage switching (ZVS) state, increasing the switching losses and electromagnetic interference, and reducing the system's efficiency. To address this issue, the three-phase-shift control method is proposed in [14] and [22]. By introducing an additional phase-shift angle between the inverter and the rectifier, the realization of ZVS on both sides can be guaranteed. However, this method increases the system's control complexity, besides, it relies on communication between the Tx and Rx sides, which is difficult to achieve in a seawater environment with long-distance power transmission.

To solve the abovementioned problem, this article introduces a constant gain frequency reduction (CGFR) module for UWPT systems with SS topology, which is able to reduce the ECL without changing the current gain of the original system, so as to improve the power efficiency. The main contributions of this article are summarized as follows.

1) An efficiency improvement strategy based on the CGFR module is proposed, the CGFR module is designed to conform to the magnetic coupler of the original system and can be easily integrated into a magnetic coupler without changing the original structure.
2) A simplified equivalent circuit of the proposed system is established, and the losses of the proposed system are analyzed, on this basis, the parameter configuration of the CGFR module is given.
3) By parameter configuration, the operating frequency of the system can be reduced, and the output current gain of the original system can be maintained unchanged without adding additional conversion circuit, communication, or control, resulting in strong universality.
4) The ECL of the original system can be reduced to improve the power efficiency, particularly in long-distance transmission scenarios where the ECL accounts for a relatively large proportion of the total power loss.

The rest of this article is organized as follows. The characteristics and ECL of UWPT system with traditional SS topology is analyzed in Section II. The principle of CGFD module is discussed in Section III. The power loss analysis and parameter configuration are given in Section IV. Subsequently, experimental results are given in Section V to validate the modeling and control methods. Finally, Section VI concludes this article.

II. UWPT SYSTEM WITH TRADITIONAL SS TOPOLOGY

A. *Circuit Analysis*

Fig. 1 shows the circuit diagram of an UWPT system with traditional SS topology, where the dc input voltage U_{in} is converted into the ac voltage $\mathbf{U_1}$ of frequency f_1 through the full-bridge inverter composed of S_1–S_4. Then, $\mathbf{U_1}$ is fed to the Tx resonant network consisting of the compensation capacitor C_1 and the Tx coil L_1 to generate a high-frequency magnetic field in the space. The Rx resonant network is composed of the compensation capacitor C_2 and the Rx coil L_2, and is placed in the same ac magnetic field. The induced ac voltage and current in the Rx coil is denoted as $\mathbf{U_2}$ and $\mathbf{I_2}$, respectively. After that, $\mathbf{I_2}$ is transferred through the full-bridge uncontrolled rectifier composed of D_1–D_4 and then filtered by the capacitor C_{f} to obtain the dc voltage U_{o} to supply the load R_{L}. Among them, R_1 and R_2 are the equivalent series ac resistances (ESRs) of the Tx coil and Rx coil, respectively. M is the mutual inductance between the Tx coil and the Rx coil.

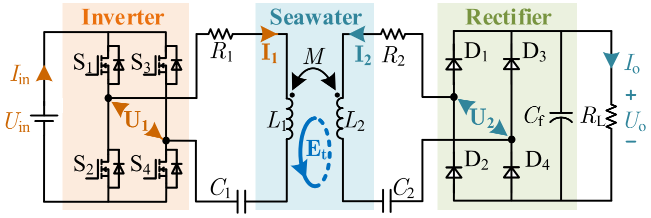

Fig. 1. UWPT system with traditional SS topology.

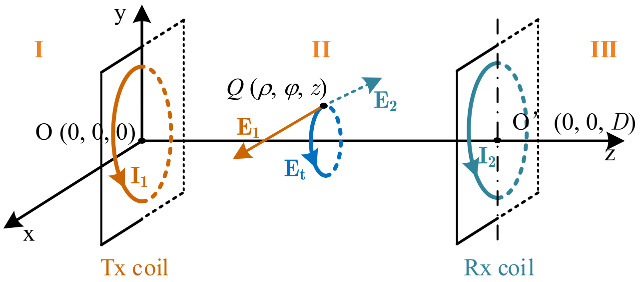

Fig. 2. Electric field distribution of UWPT system.

To simplify analysis, the ESRs are ignored. By Kirchoff's voltage law (KVL), we have

$$\begin{bmatrix} \mathbf{U_1} \\ 0 \end{bmatrix} = \begin{bmatrix} jX_1 & j\omega_1 M \\ j\omega_1 M & jX_2 + R_{\text{eq}} \end{bmatrix} \begin{bmatrix} \mathbf{I_1} \\ \mathbf{I_2} \end{bmatrix} \tag{1}$$

where $R_{\text{eq}} = 8R_{\text{L}}/\pi^2$ is the ac equivalent load resistance and $\omega_1 = 2\pi f_1$ is angular frequency. When $X_i = \omega_1 L_i - 1/\omega_1 C_i = 0$ $(i = 1, 2)$ is met, $\mathbf{I_1}$ and $\mathbf{I_2}$ can be derived as

$$\begin{cases} \mathbf{I_1} = \frac{R_{\text{eq}}}{\omega_1^2 M^2} \mathbf{U_1} \\ \mathbf{I_2} = \frac{1}{j\omega_1 M} \mathbf{U_1}. \end{cases} \tag{2}$$

B. *ECL Analysis*

UWPT systems are in the seawater and the conductivity of seawater leads to the problem ECL, which becomes more obvious when the transmission distance increases. Therefore, to improve the system efficiency, we need to first analyze the factors that dominate the ECL. Fig. 2 shows the electric field distribution of the UWPT system, where $\mathbf{E_1}$ and $\mathbf{E_2}$ are electric field generated by Tx coil and Rx coil, respectively, $\mathbf{E_t} = \mathbf{E_1} + \mathbf{E_2}$ is the synthetic electric field, Q (ρ, φ, z) is any point within region II,

D is the specifically denotes the axial center-to-center distance between the Tx and Rx coils, i.e., the transmission distance. Practically, ferrites are mounted on the outer sides of the Tx coil and Rx coil to enhance the coupling between Tx and Rx coils. Therefore, the magnetic induction strength in regions I and III is nearly zero and can be ignored. According to [16], it is assumed that the medium in region II is linearly distributed, isotropic, uniform, and unbounded, then $\mathbf{E_1}$ and $\mathbf{E_2}$ can be expressed as

$$\begin{cases} \mathbf{E_1}\left(\rho,\varphi,z\right) = -\frac{j\omega\mu r_1 N_1 I_1}{2}\int_0^\infty \frac{\lambda}{u} J_1\left(\lambda r_1\right) J_1\left(\lambda\rho\right) e^{-u|z|} \mathrm{d}\lambda \mathbf{e}_\varphi \\ \mathbf{E_2}\left(\rho,\varphi,z\right) = -\frac{j\omega\mu r_2 N_2 I_2}{2}\int_0^\infty \frac{\lambda}{u} J_1\left(\lambda r_2\right) \\ \qquad J_1\left(\lambda\rho\right) e^{-u|D-z|} \mathrm{d}\lambda \mathbf{e}_\varphi \end{cases} \tag{3}$$

where μ is permeability, r_i $(i = 1, 2)$ is radius of coils, N_i $(i = 1, 2)$ is turns of coils, λ is spatial period, J_1 is the first species first-order Bessel function, and u is a function of λ, permittivity ε, and conductivity σ described by

$$u = \sqrt{\lambda^2 - \omega\mu(\omega\varepsilon - j\sigma)}. \tag{4}$$

Due to the nonzero conductivity of seawater, $\mathbf{E_1}$ and $\mathbf{E_2}$ generate eddy current, and the resulting ECL, denoted by P_{eddy}, is

$$\begin{aligned} P_{\mathrm{eddy}} &= \iiint_V \sigma|\mathbf{E_t}|^2 \mathrm{d}V \\ &= \iiint_V \sigma|\mathbf{E_1}+\mathbf{E_2}|^2 \mathrm{d}V \\ &= \iiint_V \sigma\left({E_1}^2 + {E_2}^2 + 2E_1E_2\cos\alpha\right)\mathrm{d}V \end{aligned} \tag{5}$$

where α is the phase difference between $\mathbf{E_1}$ and $\mathbf{E_2}$. Subsequently, let us conduct a quantitative analysis of the ECL based on equivalent transformation. From (5), it can be seen that P_{eddy} consists in three parts: P_{eddy1} generated by the Tx coil, P_{eddy2} generated by the Rx coil, and P_{eddy12} generated by the coupling of both. Since $\mathbf{E_1}$ and $\mathbf{E_2}$ almost lags $\mathbf{I_1}$ and $\mathbf{I_2}$ by similarly degrees, the phase difference between $\mathbf{I_1}$ and $\mathbf{I_2}$ can be approximated as α [14] [16]. Substituting (3) into (5), we have

$$P_{\mathrm{eddy}} = \beta_1 I_1^2 f_1^2 + \beta_2 I_2^2 f_1^2 + \beta_{12} I_1 I_2 f_1^2 \cos\alpha \tag{6}$$

where

$$\begin{cases} \beta_1 = \sigma\pi^2\mu^2 r_1^2 N_1^2 \iiint_V A_1^2 \mathrm{d}V \\ \beta_2 = \sigma\pi^2\mu^2 r_2^2 N_2^2 \iiint_V A_2^2 \mathrm{d}V \\ \beta_{12} = 2\sigma\pi^2\mu^2 r_1 r_2 N_1 N_2 \iiint_V A_1 A_2 \mathrm{d}V \\ A_1 = \int_0^\infty \frac{\lambda}{u} J_1\left(\lambda r_1\right) J_1\left(\lambda\rho\right) e^{-u|z|} \mathrm{d}\lambda \mathrm{e}_\varphi \\ A_2 = \int_0^\infty \frac{\lambda}{u} J_1\left(\lambda r_2\right) J_1\left(\lambda\rho\right) e^{-u|D-z|} \mathrm{d}\lambda \mathrm{e}_\varphi. \end{cases} \tag{7}$$

From (6) and (7), it can be seen that ECL is related to various parameters, which can be divided into the following four categories.

1) Electromagnetic parameters of seawater λ, σ, μ, ε.
2) Spatial distribution parameters D, $\mathrm{d}V$.
3) Pad parameters N_1, N_2, r_1, r_2.
4) Circuit parameters f, I_1, I_2, α.

TABLE I
PARAMETERS OF PROTOTYPE

Item	Symbol	Value
Common parameters		
Input dc voltage	U_{in}	100 V
Desired output current	I_{oref}	12 A
Load resistance	R_{L}	$5 \sim 12\ \Omega$
Self-inductance of L_1	L_1	81.5 μH
Self-inductance of L_2	L_2	85.8 μH
DC ESR of Tx coil	R_{dc1}	0.019 Ω
DC ESR of Rx coil	R_{dc2}	0.019 Ω
ECL coefficient of Tx pad	β_1	1.45×10^{-11}
ECL coefficient of Rx pad	β_2	1.45×10^{-11}
Parameters of original system		
Switching frequency	f_1	180 kHz
Mutual inductance	M	6.07 μH
Coupling coefficient	k	0.07
Parameters of system with CRFR module		
Self-inductance of the CGFR coil	L_3	69.9 μH
Mutual inductance between L_1 and L_2	M_{12}	5.98 μH
Mutual inductance between L_1 and L_3	M_{13}	68.0 μH
Mutual inductance between L_2 and L_3	M_{23}	6.07 μH
DC ESR of CGFR coil	R_{dc3}	0.017 Ω

Once the operating conditions of the system are determined, the electromagnetic parameters of seawater and spatial distribution parameters can be considered fixed in the subsequent optimization process. Since the pad parameters are always fixed in practical applications, from (7), it is evident that β_1, β_2, and β_{12} remain constant no matter how f_1 changes. In this regard, it can be inferred that a reasonable way to reduce ECL is to optimize the circuit parameters.

From (2), for the UWPT systems with traditional SS topology in tuning, it is found that $\alpha = 90^\circ$ and I_2 remains unchanged when the current gain is constant. Moreover, if the input impedance has a zero phase angle (ZPA), I_1 will also remain unchanged. According to (6), we have $P_{\mathrm{eddy}} \propto f_1^2$, indicating that ECL can be decreased by reducing f_1. However, it should be noted that a decrease in f_1 will lead to an increase in I_2. In other words, if the operated frequency f_1 is reduced, this conventional system cannot maintain a CC gain without adding additional circuits or control measures, and this issue will be addressed in the following section.

III. CGFR MODULE

A. *Structure of CGFR Module*

For the system described in Fig. 1 (see Table I for the system parameters), this article proposes a novel CGFR module (see Fig. 3) to reduce the ECL while ensuring a CC gain irrespective of f_1. The rationale behind the proposed module is to reduce the operating frequency of the system.

The CGFR module comprises an inductor L_3 and a capacitor C_3 connected in series. L_3 is wound on the upper layer of L_1 and has the same parameters than L_1, i.e., $N_1 = N_3$ and $r_1 = r_3$. If we ignore the height difference caused by the wire diameter, the

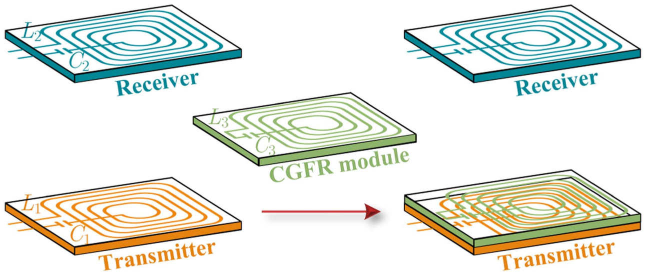

Fig. 3. Structure of the magnetic coupler with CGFR module.

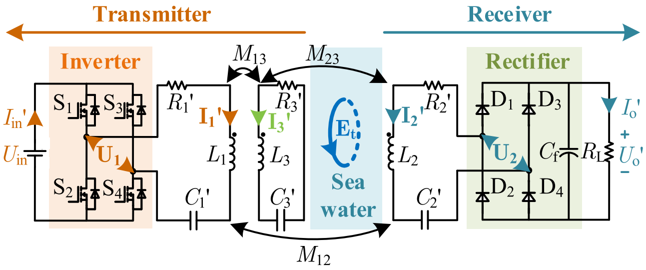

Fig. 4. Equivalent circuit diagram of UWPT systems with CGFR module.

spatial positions of L_1 and L_3 can be viewed as the same, i.e., $M_{12} \approx M_{23} \approx M$.

It should be emphasized that different from the traditional relay coil or three-coil structure, the coils in the CGFR module proposed in this article must be closely attached to the magnetic coupler of the original system and have the same geometric shape. The reasons will be explained in the Section III-C.

B. Frequency Reduction Strategy Based on CGFR Module

For an existing system, one can simply place the CGFR module on the Tx coil of the magnetic coupler to obtain a new system; see Fig. 4 for the circuit diagram. Again, to simplify the analysis, the ESRs are ignored. The KVL equation is

$$\begin{bmatrix}\mathbf{U_1}\\0\\0\end{bmatrix}=\begin{bmatrix}jX_1' & j\omega_2M_{12} & j\omega_2M_{13}\\ j\omega_2M_{12} & jX_2'+R_{\mathrm{eq}} & j\omega_2M_{23}\\ j\omega_2M_{13} & j\omega_2M_{23} & jX_3'\end{bmatrix}\begin{bmatrix}\mathbf{I_1'}\\\mathbf{I_2'}\\\mathbf{I_3'}\end{bmatrix} \tag{8}$$

where

$$\omega_2=\omega_1/n \tag{9}$$

where n is the frequency reduction ratio. That is, the CGFR module reduces the operating frequency of the system to n times that of the original system, and n can be any real number within the range $(1, +\infty)$.

When the circuit component parameters are selected such that

$$\begin{cases}X_3'=-\frac{\omega_2M_{13}M_{23}}{(n-1)M_{12}}\\ X_1'=\frac{\omega_2^2M_{13}^2}{X_3'}\quad X_2'=\frac{\omega_2^2M_{23}^2}{X_3'}\end{cases} \tag{10}$$

where

$$X_i'=\omega_2L_i-\frac{1}{\omega_2C_i'} \tag{11}$$

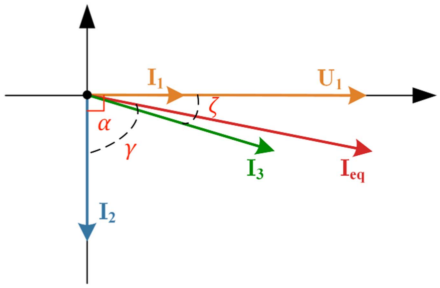

Fig. 5. Phasor diagram of the UWPT systems with CGFR module.

then we have

$$\begin{cases}\mathbf{I_1'}=\frac{R_{\mathrm{eq}}}{n^2\omega_2^2M_{12}^2}\mathbf{U_1}\\ \mathbf{I_2'}=\frac{1}{jn\omega_2M_{12}}\mathbf{U_1}\\ \mathbf{I_3'}=\left[\frac{(n-1)R_{\mathrm{eq}}}{n^2\omega_2^2M_{12}M_{23}}-j\frac{n-1}{n\omega_2M_{13}}\right]\mathbf{U_1}.\end{cases} \tag{12}$$

By substituting (9) to (12), we have

$$\begin{cases}\mathbf{I_1'}=\frac{R_{\mathrm{eq}}}{\omega_1^2M_{12}^2}\mathbf{U_1}\\ \quad\approx\frac{R_{\mathrm{eq}}}{\omega_1^2M^2}\mathbf{U_1}=\mathbf{I_1}\\ \mathbf{I_2'}=\frac{1}{j\omega_1M_{12}}\mathbf{U_1}\\ \quad\approx\frac{1}{j\omega_1M}\mathbf{U_1}=\mathbf{I_2}.\end{cases} \tag{13}$$

From (9) and (13), it can be seen that $\mathbf{I_1}=\mathbf{I_1'}$, $\mathbf{I_2}=\mathbf{I_2'}$, that is, the CGFR module reduces the operating frequency of the system to n times that of the original system, while the current gain remains constant. The phase domain behavior, as derived from (12), is visualized in the reconstructed phasor diagram (see Fig. 5), $\mathbf{U_1}$ is in phase with $\mathbf{I_1'}$ confirms preserved ZPA operation.

C. ECL Analysis of UWPT Systems With CGFR Module

This section will introduce the principle of how the CGFR module can reduce the ECL of UWPT system. The electric field $\mathbf{E_1'}$ generated by $\mathbf{I_1'}$ flowing through L_1 and $\mathbf{E_3'}$ generated by $\mathbf{I_3}$ flowing through L_3 can be expressed as

$$\begin{cases}\mathbf{E_1'}\left(\rho,\varphi,z\right)=-\frac{j\omega_2\mu r_1N_1I_1'}{2}\int_0^\infty\frac{\lambda}{u}J_1\left(\lambda r_1\right)J_1\left(\lambda\rho\right)e^{-u|z|}\mathrm{d}\lambda\mathbf{e}_\varphi\\ \mathbf{E_3'}\left(\rho,\varphi,z\right)=-\frac{j\omega_2\mu r_3N_3I_3'}{2}\int_0^\infty\frac{\lambda}{u}J_1\left(\lambda r_3\right)J_1\left(\lambda\rho\right)e^{-u|z|}\mathrm{d}\lambda\mathbf{e}_\varphi.\end{cases} \tag{14}$$

Therefore, the total ECL P_{eddy1}' generated by L_1 and L_3 can be described by

$$P_{\mathrm{eddy1}}'=\iiint_V\sigma\left({E_1'}^2+{E_3'}^2+2E_1'E_3'\cos\zeta\right)\mathrm{d}V \tag{15}$$

where ζ is the phase difference between $\mathbf{I_1'}$ and $\mathbf{I_3'}$, which can be derived from (12) as follows:

$$\begin{aligned}\zeta&=0^\circ-\arctan\frac{\mathrm{Im}(\mathbf{I_3'})}{\mathrm{Re}(\mathbf{I_3'})}\\&=\arctan\frac{\omega_1M_{12}M_{23}}{R_{\mathrm{eq}}M_{13}}.\end{aligned} \tag{16}$$

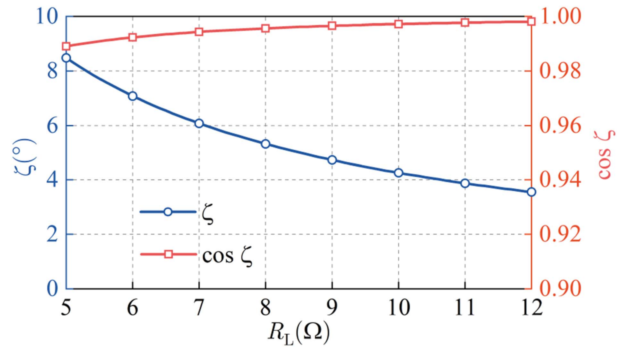

Fig. 6. ζ and $\cos\zeta$ versus R_{L}.

From (16), it is found that ζ is independent of n. ζ and $\cos\zeta$ versus R_{L} are compared in Fig. 6, from which, we have $\cos\zeta \approx 1$. Similar to (7), (15) can be reformulated as

$$P'_{\text{eddy1}} = \beta_1 I_1'^2 f_2^2 + \beta_3 I_3'^2 f_2^2 + \beta_{13} I_1' I_3' f_2^2 \cos\zeta \tag{17}$$

where

$$\begin{cases} \beta_1 = \sigma\pi^2\mu^2 r_1^2 N_1^2 \iiint_V A_1^2 \mathrm{d}V \\ \beta_3 = \sigma\pi^2\mu^2 r_3^2 N_3^2 \iiint_V A_3^2 \mathrm{d}V \\ \beta_{13} = 2\sigma\pi^2\mu^2 r_1 r_3 N_1 N_3 \iiint_V A_1 A_3 \mathrm{d}V \\ A_1 = \int_0^\infty \frac{\lambda}{u} J_1(\lambda r_1) J_1(\lambda\rho) e^{-u|z|} \mathrm{d}\lambda \mathrm{e}_\varphi \\ A_3 = \int_0^\infty \frac{\lambda}{u} J_1(\lambda r_3) J_1(\lambda\rho) e^{-u|z|} \mathrm{d}\lambda \mathrm{e}_\varphi . \end{cases} \tag{18}$$

Since the parameters of L_3 of the introduced CGFR module are the same with those of L_1 of the original system, i.e., $N_1 = N_3$ and $r_1 = r_3$, we have $\beta_{13} = 2\beta_1 = 2\beta_3$. Thus, (17) can be rewritten as

$$P'_{\text{eddy1}} = \beta_1 \left(I_1'^2 + 2 I_1' I_3' + I_3'^2 \right) f_2^2 . \tag{19}$$

It is indicated that the total electric field generated by $\mathbf{I_1'}$ flowing through L_1 and $\mathbf{I_3'}$ flowing through L_3 can be viewed as that generated by the equivalent current $\mathbf{I_{eq}} = \mathbf{I_1'} + \mathbf{I_3'}$ flowing through L_1. According to (3)–(6), the ECL of the UWPT system with CGFR module is

$$\begin{aligned} P'_{\text{eddy}} &= P'_{\text{eddy1}} + P'_{\text{eddy2}} + P'_{\text{eddy12}} \\ &= \beta_1 I_{\text{eq}}^2 f_2^2 + \beta_2 I_2'^2 f_2^2 + \beta_{12} I_{\text{eq}} I_2' f_2^2 \cos\gamma \end{aligned} \tag{20}$$

where γ is the phase difference between $\mathbf{I_{eq}}$ and $\mathbf{I_2}$. From (12), we have

$$\begin{aligned} \mathbf{I_{eq}} &= \left[\frac{(n-1)R_{\text{eq}}}{n^2\omega_2^2 M_{12} M_{23}} + \frac{R_{\text{eq}}}{n^2\omega_2^2 M_{12}^2} - j\frac{n-1}{n\omega_2 M_{13}} \right] \mathbf{U_1} \\ &\approx \left(\frac{nR_{\text{eq}}}{\omega_1^2 M_{12}^2} - j\frac{n-1}{\omega_1 M_{13}} \right) \mathbf{U_1} \\ &= n\mathbf{I_1'} - j\frac{n-1}{\omega_1 M_{13}} \mathbf{U_1} \end{aligned} \tag{21}$$

$$\begin{aligned} \gamma &= \arctan\frac{\mathrm{Im}(\mathbf{I_{eq}})}{\mathrm{Re}(\mathbf{I_{eq}})} + \alpha \\ &\approx 90° - \arctan\frac{(n-1)\omega_1 M_{12}^2}{nR_{\text{eq}} M_{13}} . \end{aligned} \tag{22}$$

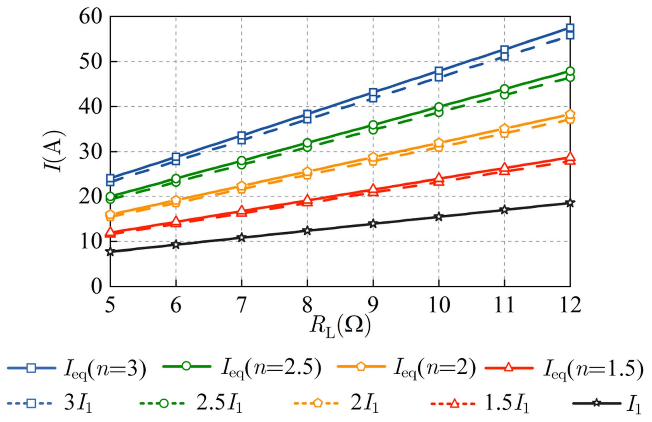

Fig. 7. I_{eq} and nI_1 versus R_{L} under different n.

1) Analysis of P'_{eddy1}: According to (21), I_{eq} and nI_1 versus R_{L} under different n are shown in Fig. 7, from which, it can seen that I_{eq} is slightly greater than nI_1, we have

$$P'_{\text{eddy1}} = \beta_1 I_{\text{eq}}'^2 f_2^2 \approx \beta_1 n^2 I_1^2 f_2^2 = \beta_1 I_1^2 f_1^2 = P_{\text{eddy1}} \tag{23}$$

which indicates that the ECL generated by Tx coils is independent of n.

2) Analysis of P'_{eddy12}: According to (22), γ and $\cos\gamma$ versus R_{L} under different n are shown in Fig. 8, from which, it can seen that $\cos\gamma \approx 0$ and

$$P'_{\text{eddy12}} = \beta_{12} I_{\text{eq}} I_2' f_2^2 \cos\gamma \approx 0 = P_{\text{eddy12}} . \tag{24}$$

3) Analysis of P'_{eddy2}: From (13), it can be seen that $I_2 = I_2'$, we have

$$P'_{\text{eddy2}} = \beta_2 I_2'^2 f_2^2 = \frac{\beta_2 I_2^2 f_1^2}{n^2} = \frac{P_{\text{eddy2}}}{n^2} \tag{25}$$

which indicates that the Rx coil ECL reduced to $1/n^2$ of the original value.

4) Analysis of P'_{eddy}: On the basis of the above analysis, the ECL of the UWPT system by taking the CGFR module into account is reduced by

$$\Delta P_{\text{eddy}} = P_{\text{eddy2}} - P'_{\text{eddy2}} . \tag{26}$$

By substituting (25) to (26), we have

$$\begin{aligned} \Delta P_{\text{eddy}} &= \frac{n^2-1}{n^2} \beta_2 I_2^2 f_1^2 \\ &= \frac{n^2-1}{n^2} P_{\text{eddy2}} . \end{aligned} \tag{27}$$

From (13) and (27), it can be seen that the CGFR module proposed in this article can reduce the ECL and the current gain of the system can be maintained unchanged without the need to add additional circuits or controls.

IV. PARAMETER CONFIGURATION OF CGFR MODULE

For a specific UWPT system with SS topology, the parameter configuration of the CGFR module essentially boils down to the selection of the frequency reduction ratio n. It can be seen from (27) that the larger n is, the smaller the ECL will be. However,

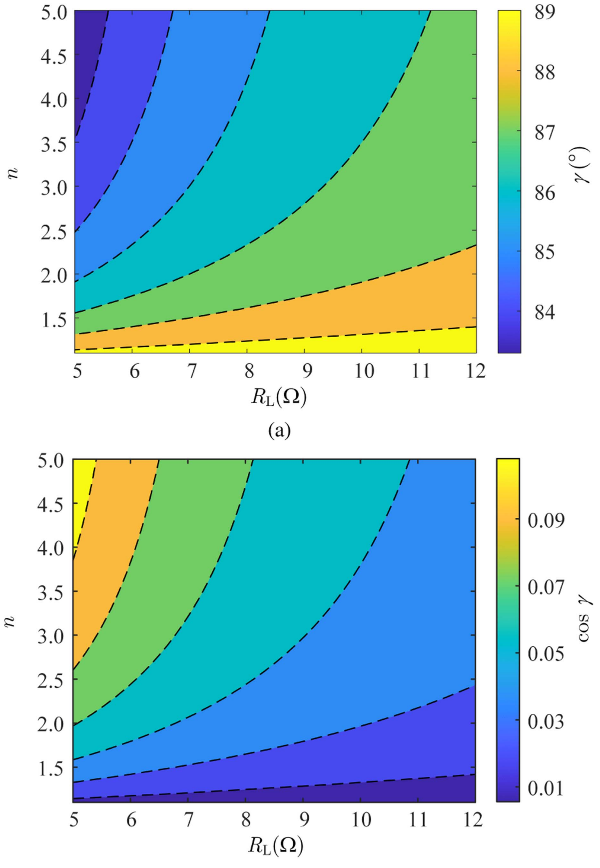

(a)

(b)

Fig. 8. γ and cos γ versus R_L under different n. (a) γ. (b) cos γ.

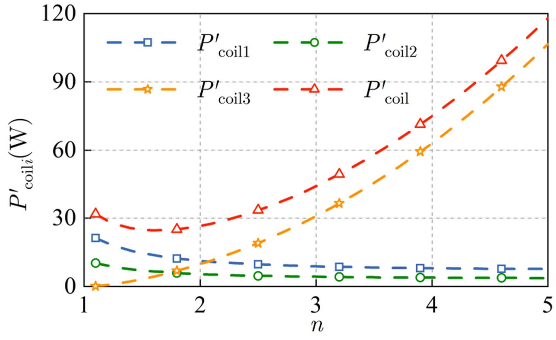

Fig. 9. Copper losses versus n under $R_L = 12\Omega$.

the CGFR module will introduce additional coil losses, so there exists an optimal n at which the best efficiency is achieved. Therefore, this section will conduct a further analysis of the relationship between the total losses of the system and n.

A. Power Losses Analysis

The overall losses P'_{loss} of the UWPT system with SS topology mainly consists of four parts, i.e., the losses of the inverter P'_{inv}, rectifier P'_{rec}, magnetic coupler P'_{mc}, and eddy currents P'_{eddy}.

1) Power Losses of the Inverter: Since the UWPT system with the CGFR module proposed in this article does not require phase shift control, the losses of the inverter P'_{inv} can be approximately expressed by the conduction losses of MOSFETs as [23]

$$P'_{\text{inv}} = 2I'^2_1 R_{\text{inv}} \tag{28}$$

where R_{inv} is the drain-source on-state resistance.

2) Power Losses of the Rectifier: The power losses of the rectifier P'_{rec} can be given as [23]

$$P'_{\text{rec}} = \frac{4\sqrt{2}}{\pi} V_F I'_2 + 2I'^2_2 R_{\text{rec}} \tag{29}$$

where V_F is the diode forward voltage and R_{rec} is the equivalent on-state resistance of diode.

3) Power Losses of the Magnetic Coupler: Since the magnetic coupler in this article does not contain aluminum plate, the losses of the magnetic coupler P'_{mc} can be divided into two parts: the core losses P'_{core} introduced by the ferrite layers and the copper losses P'_{coil} introduced by the coil layers. Thus, we have

$$P'_{\text{mc}} = P'_{\text{core}} + P'_{\text{coil}}. \tag{30}$$

The total core losses P'_{core} can be expressed as

$$P'_{\text{core}} = c{f_2}^a {B'_1}^b V_1 + c{f_2}^a {B'_2}^b V_2 \tag{31}$$

where a, b, c are empirical coefficients, which can be obtained from the ferrite datasheet, B'_1 and B'_2 are the magnetic flux densities within the Tx ferrite layer and Rx ferrite layer, respectively. V_1 and V_2 are the volumes of the Tx ferrite layer and Rx ferrite layer, respectively. Although the core loss varies as a function of n, it is normally ver small and seldom affects the total losses. Therefore, for simplicity in analysis, it can be approximated as a constant [24].

The copper losses P'_{coil} can be described as

$$P'_{\text{coil}} = {I'_1}^2 R'_1 + {I'_2}^2 R'_2 + {I'_3}^2 R'_3 \tag{32}$$

where $R'_i (i = 1, 2, 3)$ are the ac ESRs of the coils within f_2. Although the litz wire, which consists of many copper strands, can be applied to reduce the skin and proximity effects, the improvement is limited for high-frequency operation. Therefore, for a more accurate calculation of P'_{coil}, R'_i can be described as [25]

$$R'_i = R_{\text{dc}i}\left[1 + \frac{5N^2 - 1}{45}\left(\frac{\pi}{4}\right)^3 \left(\frac{d}{p'}\right)^4\right] \tag{33}$$

where $R_{\text{dc}i}$ is the dc ESRs of the coils, d is the diameter of the litz wire, N is the total effective number of copper strands of the coil, and p' is the skin depth of the litz wire, which can be expressed as

$$p' = \frac{1}{\sqrt{\pi \mu_0 \sigma_{\text{cu}} f_2}} \tag{34}$$

where μ_0 is the vacuum permeability and σ_{cu} is the conductivity of the copper. Coil losses versus n under R_L =12 Ω are shown in Fig. 9, from which, it can been seen that the lager n is, the smaller copper losses of Tx coil P'_{coil1} and Rx coil P'_{coil2} are.

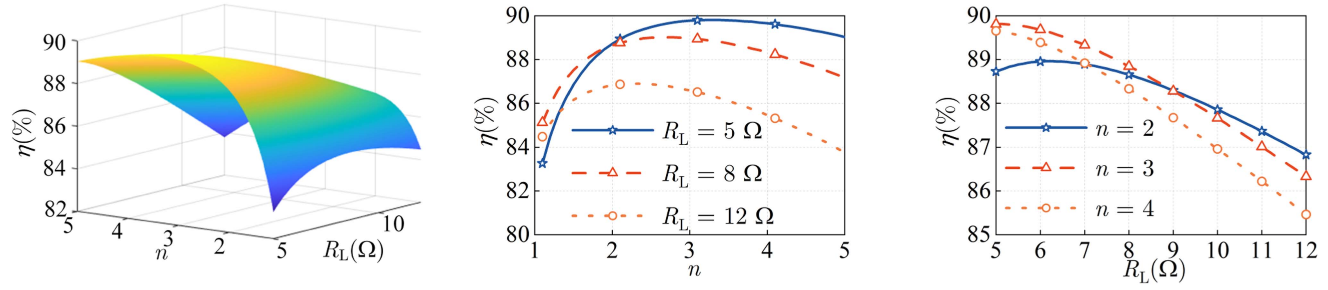

(a) (b) (c)

Fig. 10. DC–DC efficiency η versus R_L and n. (a) Three dimension. (b) η versus n. (c) η versus R_L.

However, since the copper loss of the CGFR module coil P'_coil3 will increase as n increases, the total copper loss P'_coil will first decrease and then increase.

4) Power Losses of the Eddy Currents: The ECL of the UWPT system with CGFR module has been analyzed in detail in Section III-C, showing that the larger n is, the smaller the P'_eddy is. According to (24), it can be calculated by

$$P'_\mathrm{eddy} = \beta_1 I_\mathrm{eq}^2 f_2^2 + \beta_2 I_2'^2 f_2^2. \tag{35}$$

B. How to Select Frequency Reduction Ratio n

This article focuses on improving the efficiency of the UWPT system. Therefore, efficiency is the most crucial indicator for the selection of n. In addition, the device stress in the system is also a constraint. As seen from (13), the currents in the Tx and Rx coils of the UWPT system with the CGFR module are independent of n and remain the same as those in the original system. Thus, the device stresses of the inverter, L_1, L_2, and the rectifier do not change. However, as indicated by (12), the current flowing through L_3 increases with the increase of n. An excessively large n will lead to an overly high current stress on L_3. Therefore, based on the maximum overcurrent capacity of the adopted litz wire, when R_L reaches its maximum value, the upper limit of n can be calculated through (12).

The dc–dc transmission efficiency η of the UWPT system with the CGFR module can be computed as

$$\eta = \frac{I_\mathrm{o}'^2 R_\mathrm{L}}{I_\mathrm{o}'^2 R_\mathrm{L} + P'_\mathrm{loss}} \times 100\%. \tag{36}$$

According to (28)–(36), η versus n and R_L are shown in Fig. 10, from which, it can be seen that for each R_L, there exists an optimal frequency reduction multiple n_o that maximizes the η. When R_L is in the range of 5–12 Ω, the optimal n is 2–4. Since the SS topology addressed in this article has the characteristic of CC output, the larger R_L is, the greater the output power is. From Fig. 10(c), it can be seen that when the system is operating under a light load condition, the efficiency with $n = 3$ is higher, when the system is operating under a heavy load condition, the efficiency with $n = 2$ is higher. In addition, it can be observed that when $n = 3$, the system's efficiency fluctuates less within the load range of 5–12 Ω.

Since η is dependent on R_L, which could vary with respect to time, let us define a weighted efficiency ξ as follows as a new performance index

$$\xi = \sum_{i=1}^{m} w_i \eta_i \tag{37}$$

where w_i and η_i are, respectively, the weight and efficiency when the load is $R_{\mathrm{L}i}$, m is the number of load levels. When adopting the CGFR module to improve the transmission efficiency of the UWPT system, different weights can be assigned to different load levels according to the actual requirements, and it needs to satisfy

$$\sum_{i=1}^{m} w_i = 1. \tag{38}$$

By calculating with (37), the value of n that maximizes ξ is selected as the frequency reduction ratio of the system. Then, the corresponding values of the compensation capacitances are determined according to (10) and (11), thus completing the parameter configuration of the CGFR module. The procedure is summarized in Fig. 11.

V. EXPERIMENTAL VERIFICATION

A. Experimental Setup

A 1.5-kW prototype was constructed to experimentally validate the efficiency enhancement of the proposed methodology (see Fig. 12). A comparative experimental evaluation was conducted at frequency reduction ratios $n = 2$ and $n = 3$, with critical system parameters enumerated in Table II. Both Tx and Rx coils measure 300 × 300 mm, wound with 12-turn litz wire ($N_1 = N_2 = N_3 = 12$), and the Tx and Rx ferrite sizes are both 300 × 300 × 10 mm. The gap between Tx and Rx is 200 mm, which is filled with seawater of $\sigma = 4.8$ S/m [14]. The MOSFETs of the full-bridge inverter are C3M0021120K from Wolfspeed, and the diodes of the full-bridge rectifier are IDWD30G120C5 from Infineon. The TMS320F28335 processor serves as the controller.

B. CC and Constant Gain Performance Verification

Fig. 13 shows the output currents with different loads. Under the condition of same U_in, the output current I'_o with $n = 2$, I'_o

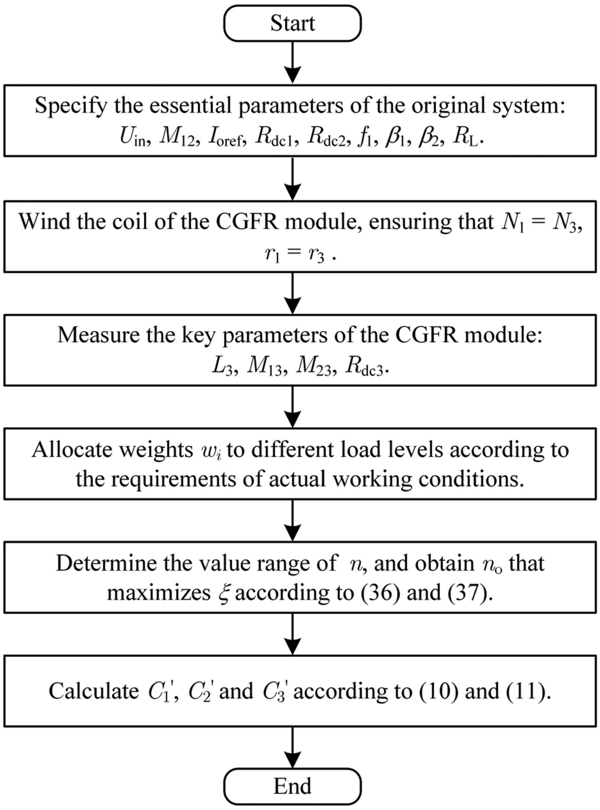

Fig. 11. Flowchart of the parameter configuration of the CGFR module procedure.

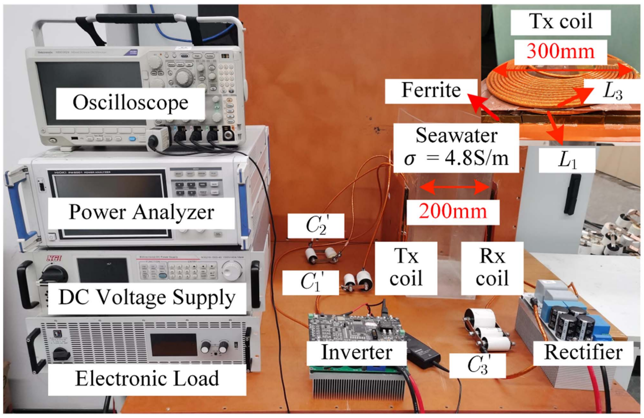

Fig. 12. Experimental prototype.

with $n = 3$, and I_{o} are almost consistent, which indicates that the CGFD module proposed in this article will not change the current gain of the system. Besides, it has CC output characteristics within the load variation range from 5 to 12 Ω.

Fig. 14 shows the experimental waveforms with different loads. It can be seen that the frequency of the proposed system is reduced by n compared with that of the original system. Moreover, I_{eq} is almost equal to nI_1, which verifies the conclusion in Section III-C, and that the ECL generated by the Tx remains unchanged under the three different experimental conditions.

TABLE II
PARAMETERS OF PROTOTYPE

Item	Symbol	Value
Parameters of the original system		
Switching frequency	f_1	180 kHz
Compensation capacitor of L_1	C_1	9.46 nF
Compensation capacitor of L_2	C_2	9.06 nF
Parameters of CGFR module with $n = 2$		
Switching frequency	f_2	90 kHz
Compensation capacitor of L_1	C_1'	21.8 nF
Compensation capacitor of L_2	C_2'	36.3 nF
Compensation capacitor of L_3	C_3'	22.7 nF
Parameters of CGFR module with $n = 3$		
Switching frequency	f_3	60 kHz
Compensation capacitor of L_1	C_1''	32.4 nF
Compensation capacitor of L_2	C_2''	81.2 nF
Compensation capacitor of L_3	C_3''	66.7 nF

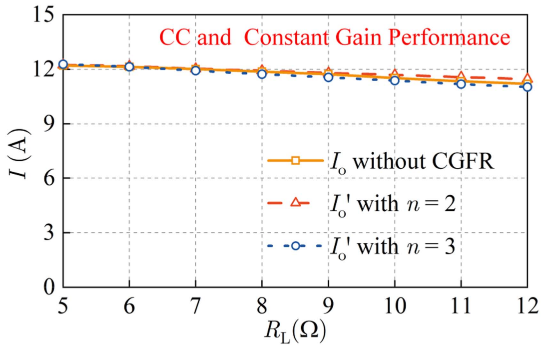

Fig. 13. I_{o} and I_{o}' versus R_{L}.

Besides, the topology proposed in this article provides a relatively larger phase lag in the resonant current than the traditional topology, which helps to achieve the ZVS operation and further improve the transmission efficiency, especially in the presence of heavier harmonic distortions.

C. Efficiency Improvement Strategy Verification

Fig. 15 compares the efficiency η_{mea} measured by power analyzer PW6001 from HIOKI and η_{cal} calculated by (36) of the three systems with different loads. It should be noted that η_{cal} is calculated by substituting the current measured by the current probe into (36). It is clear from this figure that η_{mea} and η_{cal} are almost equal, which verifies the accuracy of (36).

It can also be seen from Fig. 15 that the efficiency of the two systems using the CGFR module is higher than that of the original system within the load range of 5 to 12 Ω. Particularly, the efficiency attains its peak value at $n = 3$ in the light load condition, while at $n = 2$ in the heavy load condition. In addition, the fluctuation of the transmission efficiency of the system with $n = 2$ is relatively small when the load changes.

The input and output parameters of the three systems when $R_{\mathrm{L}} = 5\ \Omega$ and $R_{\mathrm{L}} = 12\ \Omega$ measured by power analyzer are

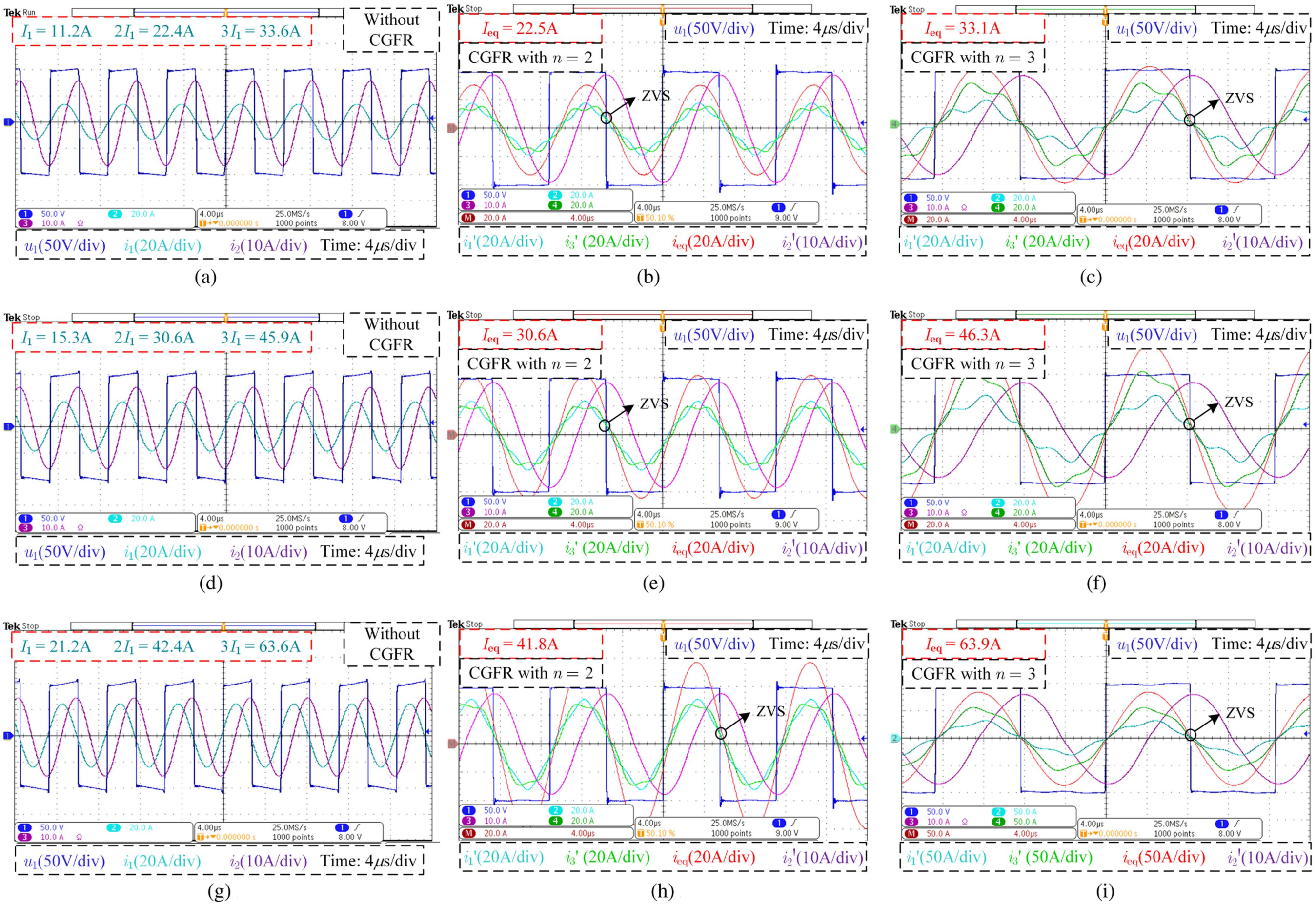

(a) (b) (c)

(d) (e) (f)

(g) (h) (i)

Fig. 14. Experimental waveforms with different R_L. (a), (d), and (g) Without CGFR. (b), (e), and (h) $n = 2$. (c), (f), and (i) $n = 3$. (a) $R_\mathrm{L} = 5\ \Omega$. (b) $R_\mathrm{L} = 5\ \Omega$. (c) $R_\mathrm{L} = 5\ \Omega$. (d) $R_\mathrm{L} = 8\ \Omega$. (e) $R_\mathrm{L} = 8\ \Omega$. (f) $R_\mathrm{L} = 8\ \Omega$. (g) $R_\mathrm{L} = 12\ \Omega$. (h) $R_\mathrm{L} = 12\ \Omega$. (i) $R_\mathrm{L} = 12\ \Omega$.

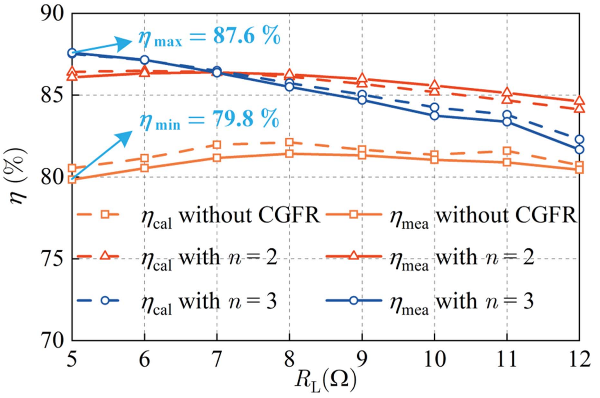

Fig. 15. η_cal and η_mea versus R_L.

shown in Fig. 16, from which, it can be seen that the efficiency of the system with $n = 3$ increases from 79.8% to 87.6%, with a maximum improvement of 7.8% when $R_\mathrm{L} = 5\ \Omega$, and the efficiency of the system with $n = 2$ increases from 80.4% to 84.6%, with a maximum improvement of 4.2% when $R_\mathrm{L} = 12\ \Omega$. It is indicated that the CGFR module proposed in this article can improve the efficiency of the UWPT system without changing the current gain.

Notably, as additionally demonstrated in Fig. 15, the maximum efficiency improvement occurs under light-load conditions. The UWPT system with SS-compensated topology adopted in this article exhibits a load-independent CC output characteristic, that is, the larger R_L is, the greater output power P_out will be. However, due to the inherent CC output characteristic of the system, the ECL generated by the Rx side remain load-independent. Consequently, the proportion of Rx side ECL in total system losses decreases with increasing load resistance. Crucially, since the proposed strategy enhances efficiency by suppressing Rx ECL (as analyzed in Section III-C), the maximum efficiency improvement is achieved under light-load conditions.

D. Power Losses Analysis

Fig. 17 shows the loss distribution of the three systems when $R_\mathrm{L} = 5\ \Omega$ and $R_\mathrm{L} = 12\ \Omega$. It can be seen that since $I_1 \approx I_1'$ and $I_2 \approx I_2'$, P_inv, P_rec, P_coil1, and P_coil2 of the three systems are almost unchanged. However, the system with the CGFR module has an additional coil loss $P_{\mathrm{coil}3'}$. Moreover, it can be

TABLE III
COMPARISONS WITH OTHER WORKS

References	Strategy	Power and efficiency	Coupling coefficient k	Maximum efficiency improvement	Wireless communication	Complexity	Universality
[12]	Magnetic coupler design	80 – 300 W 71 – 79 %	0.1	9 %	No	✦✦✦✦✧	★★☆☆☆
[14]	Phase-shift control	2.3 kW(85.5 %)	0.22	7.46 %	Required	✦✦✦✦✧	★★★☆☆
[15]	Frequency control	200 W(88 %)	0.19	4 %	No	✦✦✧✧✧	★★★★★
This article	**CGFR module**	**0.8 – 1.58 kW** **81.7 – 87.6 %**	**0.07**	**7.8 %**	**No**	✦✦✦✧✧	★★★★★

Notes: ✦ represents the complexity level of the system. The more ✦, the higher the complexity of the system.
★ represents the universality level of the system. The more ★, the higher the universality of the system.
The bold values highlight the key metrics in our study.

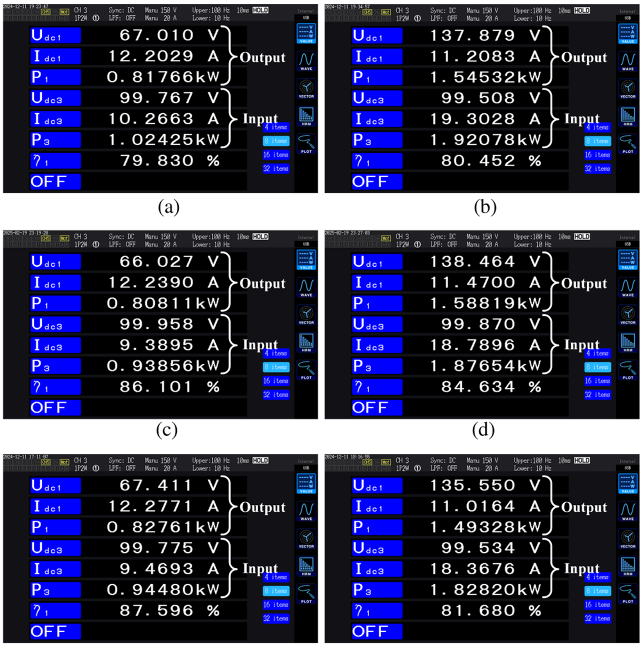

```
Udc1   67.010 V
Idc1   12.2029 A    Output
P1     0.81766kW
Udc3   99.767 V
Idc3   10.2663 A    Input
P3     1.02425kW
η1     79.830 %
OFF
```

(a)

```
Udc1   137.879 V
Idc1   11.2083 A    Output
P1     1.54532kW
Udc3   99.508 V
Idc3   19.3028 A    Input
P3     1.92078kW
η1     80.452 %
OFF
```

(b)

```
Udc1   66.027 V
Idc1   12.2390 A    Output
P1     0.80811kW
Udc3   99.958 V
Idc3   9.3895 A     Input
P3     0.93856kW
η1     86.101 %
OFF
```

(c)

```
Udc1   138.464 V
Idc1   11.4700 A    Output
P1     1.58819kW
Udc3   99.870 V
Idc3   18.7896 A    Input
P3     1.87654kW
η1     84.634 %
OFF
```

(d)

```
Udc1   67.411 V
Idc1   12.2771 A    Output
P1     0.82761kW
Udc3   99.775 V
Idc3   9.4693 A     Input
P3     0.94480kW
η1     87.596 %
OFF
```

(e)

```
Udc1   135.550 V
Idc1   11.0164 A    Output
P1     1.49328kW
Udc3   99.534 V
Idc3   18.3676 A    Input
P3     1.82820kW
η1     81.680 %
OFF
```

(f)

Fig. 16. Power Meter. (a), (b) without CGFR. (c), (d) $n = 2$. (e), (f) $n = 3$. (a) $R_L = 5\ \Omega$. (b) $R_L = 12\ \Omega$. (c) $R_L = 5\ \Omega$. (d) $R_L = 12\ \Omega$. (e) $R_L = 5\ \Omega$. (f) $R_L = 12\ \Omega$.

seen that the ECL generated by Tx P_{eddy1} of the three systems are almost equal. However, the ECL generated by Rx P_{eddy2} of the system with CGFR module are almost reduced by n^2 times, which agrees well with (27). Therefore, the transmission efficiency is improved.

E. Comparison With Other Works

Table III gives a comparison of this work with existing research works that focus on efficiency improvement for UWPT systems. In [12], a $1 \times 1 \times 1$ magnetic coupler is proposed, which can reduce by half the Tx coil ECL. However, this method cannot be applied to situations where the Rx coil uses ferrite. In [14], the ECL can be reduced by suitably adjusting the phase difference between the currents flowing through Tx and Rx coils. Nevertheless, an active rectifier is required on the Rx side. In [15], the efficiency can be improved by optimizing the operating frequency of the system. Nevertheless, the method does not guarantee a CC gain for UWPT systems.

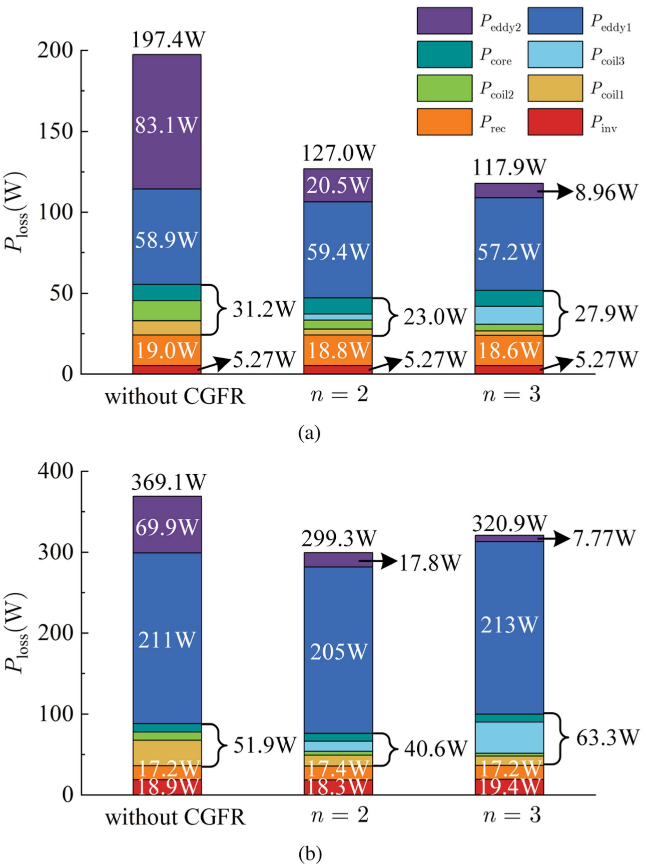

Fig. 17. Loss distribution when (a) $R_L = 5\ \Omega$. (b) $R_L = 12\ \Omega$.

To sum up, compared with other works, the strategy proposed in this article has the following three main advantages.

1) The strategy proposed in this article can significantly improve the transmission efficiency of the UWPT system within the load range of 50 % to 100 %, and there is no need to add any additional converters or control measures.
2) The strategy proposed in this article can achieve an efficiency of 87.6 % when the coupling coefficient k is only 0.07. It is indicated that the strategy has good application potential in scenarios of long-distance transmission.

3) The strategy proposed in this article does not rely on communication, and it applies to magnetic couplers of various shapes, showing good universality.

VI. CONCLUSION

An efficiency improvement strategy with CC characteristics for UWPT systems with SS topology has been proposed in this article. A CGFR module has been developed and by placing it on the Tx coil of a WPT system, the operating frequency of the system can be reduced by n times, while the ECL generated by the Rx coil can be reduced by n^2 times. In this process, the system preserves a CC gain. By establishing the circuit model of the proposed system, analyzing the losses of the system, and based on this, a parameter configuration method for the CGFR module is given. A 1.5-kW prototype is developed, and the experimental results show that the proposed CGFR module indeed improves the system efficiency within the load variation from 5 to 12 Ω, with a maximum increment of 7.8%. The proposed strategy can significantly improve the efficiency of the UWPT system, and it is particularly applicable in scenarios of long-distance transmission.

REFERENCES

[1] Z. Liu, T. Li, S. Li, and C. C. Mi, “Advancements and challenges in wireless power transfer: A comprehensive review,” *Nexus*, vol. 1, no. 2, 2024, Art. no. 100014. [Online]. Available: https://www.sciencedirect.com/science/article/pii/S2950160124000123

[2] B. Zhang, C. Q. Jiang, F. Yang, C. Chen, Y. Lu, and J. Zhou, “An antirotation wireless power transfer system with a flexible magnetic coupler for autonomous underwater vehicles,” *IEEE Trans. Power Electron.*, vol. 40, no. 1, pp. 2593–2603, Jan. 2025.

[3] A. Mostafa, Y. Wang, F. Lu, and H. Zhang, “Enhanced axial misalignment tolerance in a 10-kW autonomous underwater vehicle wireless charging system utilizing a split solenoid coupler,” *IEEE Trans. Power Electron.*, vol. 39, no. 10, pp. 12041–12046, Oct. 2024.

[4] D. Wang, F. Chen, J. Zhang, S. Cui, Z. Bie, and C. Zhu, “A novel pendulum-type magnetic coupler with high misalignment tolerance for AUV underwater wireless power transfer systems,” *IEEE Trans. Power Electron.*, vol. 38, no. 12, pp. 14861–14871, Dec. 2023.

[5] Z. Chen, X. Zhang, F. Xu, M. Li, Z. Yuan, and Q. Yang, “Wide rotation-misalignment-tolerance design of magnetic coupled structure for AUVs wireless charging system,” *IEEE Trans. Ind. Electron.*, vol. 71, no. 11, pp. 14086–14096, Nov. 2024.

[6] Z. Yan et al., “Free-rotation wireless power transfer system based on composite anti-misalignment method for AUVs,” *IEEE Trans. Power Electron.*, vol. 38, no. 4, pp. 4262–4266, Apr. 2023.

[7] H. Tang et al., “A self-adaptive dual-channel LCC-s detuned topology for misalignment tolerance in AUV wireless power transfer systems,” *IEEE Trans. Power Electron.*, vol. 40, no. 3, pp. 4630–4639, Mar. 2025.

[8] J. Li, C. Zhu, J. Xie, F. Lu, and X. Zhang, “Design and implementation of high-misalignment tolerance WPT system for underwater vehicles based on a variable inductor,” *IEEE Trans. Power Electron.*, vol. 38, no. 10, pp. 11726–11737, Oct. 2023.

[9] B. Luo et al., “Front-end parameter identification method based on adam-W optimization algorithm for underwater wireless power transfer system,” *IEEE Trans. Power Electron.*, vol. 40, no. 4, pp. 6307–6318, Apr. 2025.

[10] L. Yang et al., “Constant voltage and constant current control method of undersea wireless power supply system based on frequency tracking method,” *IEEE Trans. Power Electron.*, vol. 40, no. 4, pp. 6359–6369, Apr. 2025.

[11] X. Liu, D. Lu, Z. Liao, C. Rong, and C. Xia, “Critical and parasitic parameters identification and frequency regulation strategies for UWPT systems,” *IEEE Trans. Power Electron.*, vol. 39, no. 8, pp. 10558–10567, Aug. 2024.

[12] K. Zhang, X. Zhang, Z. Zhu, Z. Yan, B. Song, and C. C. Mi, “A new coil structure to reduce eddy current loss of WPT Systems for underwater vehicles,” *IEEE Trans. Veh. Technol.*, vol. 68, no. 1, pp. 245–253, Jan. 2019.

[13] X. Zhang, G. Li, T. Chen, F. Wang, Q. Yang, and W. Xu, “A high-efficiency underwater hybrid wireless power transfer system with low plate voltage stresses,” *IEEE Trans. Power Electron.*, vol. 39, no. 8, pp. 10546–10557, Aug. 2024.

[14] Z. Wang et al., “An optimization approach for efficiency and interoperability enhancement of WPT systems for autonomous underwater vehicles,” *IEEE Trans. Power Electron.*, vol. 40, no. 4, pp. 6345–6358, Apr. 2025.

[15] Z. Yan et al., “Frequency optimization of a loosely coupled underwater wireless power transfer system considering eddy current loss,” *IEEE Trans. Ind. Electron.*, vol. 66, no. 5, pp. 3468–3476, May 2019.

[16] K. Zhang, Y. Ma, Z. Yan, Z. Di, B. Song, and A. P. Hu, “Eddy current loss and detuning effect of seawater on wireless power transfer,” *IEEE Trans. Emerg. Sel. Topics Power Electron.*, vol. 8, no. 1, pp. 909–917, Mar. 2020.

[17] K. Song et al., “Constant current charging and maximum system efficiency tracking for wireless charging systems employing dual-side control,” *IEEE Trans. Ind. Appl.*, vol. 56, no. 1, pp. 622–634, Jan./Feb. 2020.

[18] T. Orekan, P. Zhang, and C. Shih, “Analysis, design, and maximum power-efficiency tracking for undersea wireless power transfer,” *IEEE Trans. Emerg. Sel. Topics Power Electron.*, vol. 6, no. 2, pp. 843–854, Jun. 2018.

[19] H. Li, J. Li, K. Wang, W. Chen, and X. Yang, “A maximum efficiency point tracking control scheme for wireless power transfer systems using magnetic resonant coupling,” *IEEE Trans. Power Electron.*, vol. 30, no. 7, pp. 3998–4008, Jul. 2015.

[20] Y. Jiang, L. Wang, J. Fang, C. Zhao, K. Wang, and Y. Wang, “A joint control with variable ZVS angles for dynamic efficiency optimization in wireless power transfer system,” *IEEE Trans. Power Electron.*, vol. 35, no. 10, pp. 11064–11081, Oct. 2020.

[21] Y. Li, J. Hu, F. Chen, Z. Li, Z. He, and R. Mai, “Dual-phase-shift control scheme with current-stress and efficiency optimization for wireless power transfer systems,” *IEEE Trans. Circuits Syst. I: Reg. Papers*, vol. 65, no. 9, pp. 3110–3121, Sep. 2018.

[22] X. Zhang et al., “A control strategy for efficiency optimization and wide ZVS operation range in bidirectional inductive power transfer system,” *IEEE Trans. Ind. Electron.*, vol. 66, no. 8, pp. 5958–5969, Aug. 2019.

[23] Y. Li et al., “Efficiency analysis and optimization control for input-parallel output-series wireless power transfer systems,” *IEEE Trans. Power Electron.*, vol. 35, no. 1, pp. 1074–1085, Jan. 2020.

[24] X. Liu et al., “A multi-inverter multi-rectifier wireless power transfer system for charging stations with power loss optimized control,” *IEEE Trans. Power Electron.*, vol. 38, no. 8, pp. 9261–9277, Aug. 2023.

[25] Y. Chen, H. Zhang, C.-S. Shin, C.-H. Jo, S.-J. Park, and D.-H. Kim, “An efficiency optimization-based asymmetric tuning method of double-sided LCC compensated WPT system for electric vehicles,” *IEEE Trans. Power Electron.*, vol. 35, no. 11, pp. 11475–11487, Nov. 2020.

Han Hu received the B.E. degree in automation in 2019 from Chongqing University, Chongqing, China, where he is currently working toward the Ph.D. degree in control theory and control engineering with the College of Automation.

His current research interests include underwater wireless power transfer and improving misalignment tolerance.

Hongsheng Hu (Member, IEEE) received the B.Eng. degree in electrical engineering and automation and the Ph.D. degree in power electronics and power drives from the Huazhong University of Science and Technology, Wuhan, China, in 2014 and 2021, respectively.

He is currently an Associate Professor with the School of Automation, Chongqing University, Chongqing, China. His research interests include modularized IPT systems, bidirectional IPT systems, capacitive IPT systems, and power electronics.

Fengwei Chen was born in Chongqing, China. He received the B.Eng. degree in automation and the M.Eng. degree in control theory and control engineering from Wuhan University, Wuhan, China, in 2009 and 2011, respectively, and the Ph.D. degree in automatic control from the Université de Lorraine, Nancy, France, in 2014.

From 2015 to 2016, he was a Lecturer with the Dalian University of Technology, Dalian, China. From 2017 to 2020, he was an Associate Researcher with Wuhan University, Wuhan, China. Since 2021, he has been with Chongqing University, Chongqing, China, where he is currently an Associate Professor. His research interests include system identification and parameter estimation, with applications to wireless power transfer.

Xin Dai (Member, IEEE) received the B.S. degree in industrial automation from Yuzhou University, Chongqing, China, in 2000, and the Ph.D. degree in control theory and control engineering from the School of Automation, Chongqing University, Chongqing, China, in 2006.

In 2012, he was a Visiting Scholar with The University of Auckland, Auckland, New Zealand. He is currently a Professor with the School of Automation, Chongqing University. His research interests include wireless power transfer technology and nonlinear dynamic behavior analysis of power electronics.

Yue Sun received the B.E. degree in electrical engineering, the M.E. degree in industrial automation, and the Ph.D. degree in mechanical electrical integrated manufacturing from Chongqing University, Chongqing, China, in 1982, 1988, and 1995, respectively.

In 1997, he was a Senior Visiting Scholar with the University of Valenciennes, Famars, France. He is currently a Professor with the College of Automation, Chongqing University. His current research interests include automatic control, wireless power transfer, and power electronics applications.